REPORT DOCUMENTATION PAGE

Form Approved OMB NO. 0704-0188

The public reporting burden for this collection of information is estimated to average 1 hour per response, including the time for reviewing instructions, searching existing data sources, gathering and maintaining the data needed, and completing and reviewing the collection of information. Send comments regarding this burden estimate or any other aspect of this collection of information, including suggesstions for reducing this burden, to Washington Headquarters Services, Directorate for Information Operations and Reports, 1215 Jefferson Davis Highway, Suite 1204, Arlington VA, 22202-4302. Respondents should be aware that notwithstanding any other provision of law, no person shall be subject to any oenalty for failing to comply with a collection of information if it does not display a currently valid OMB control number.
PLEASE DO NOT RETURN YOUR FORM TO THE ABOVE ADDRESS.

1. REPORT DATE (DD-MM-YYYY)	2. REPORT TYPE	3. DATES COVERED (From - To)
14-09-2007	Final Report	15-Aug-2006 - 14-Feb-2007

4. TITLE AND SUBTITLE	5a. CONTRACT NUMBER
Experimental Investigation of the Interaction of Electrothermal Plasmas with Solid Propellants	W911NF-06-1-0373
	5b. GRANT NUMBER
	5c. PROGRAM ELEMENT NUMBER
	611102

6. AUTHORS	5d. PROJECT NUMBER
Philip L. Varghese, Noel T. Clemens, Michael D. Ryan	
	5e. TASK NUMBER
	5f. WORK UNIT NUMBER

7. PERFORMING ORGANIZATION NAMES AND ADDRESSES	8. PERFORMING ORGANIZATION REPORT NUMBER
University of Texas - Austin Applied Research Laboratories The University of Texas at Austin Austin, TX 78758 -	

9. SPONSORING/MONITORING AGENCY NAME(S) AND ADDRESS(ES)	10. SPONSOR/MONITOR'S ACRONYM(S)
U.S. Army Research Office P.O. Box 12211 Research Triangle Park, NC 27709-2211	ARO
	11. SPONSOR/MONITOR'S REPORT NUMBER(S)
	51043-EG-II.1

12. DISTRIBUTION AVAILIBILITY STATEMENT

Distribution authorized to U.S. Government Agencies Only, Contains Proprietary information

13. SUPPLEMENTARY NOTES

The views, opinions and/or findings contained in this report are those of the author(s) and should not contrued as an official Department of the Army position, policy or decision, unless so designated by other documentation.

14. ABSTRACT

We report measurements of the interaction between plasma radiation and solid propellant. We made heat flux measurements of the electrothermal plasma jet impinging on a sensor mimicking a disk of propellant. We made planar laser-induced fluorescence images of NO, a JA2 decomposition product, at the propellant surface. High speed video imaging of the propellant surface and scattering of ejected particles was used to study how the propellant surface evolves during exposure to plasma radiation. During the radiation interaction scattering particles and NO appeared between 100 and 150 microseconds after the beginning of the discharge and propagated away from the propellant surface. The ejected material occurred in

15. SUBJECT TERMS

Electrothermal Plasma, Solid Propellant, JA-2, Plasma Propellant Interactions, Experimental Measurements

16. SECURITY CLASSIFICATION OF:			17. LIMITATION OF ABSTRACT	15. NUMBER OF PAGES	19a. NAME OF RESPONSIBLE PERSON
a. REPORT S	b. ABSTRACT U	c. THIS PAGE U	SAR		Philip Varghese
					19b. TELEPHONE NUMBER 512-471-3110

Standard Form 298 (Rev 8/98)
Prescribed by ANSI Std. Z39.18

Report Title

Final Report: Experimental Investigation of the Interaction of Electrothermal Plasmas with Solid Propellants

ABSTRACT

We report measurements of the interaction between plasma radiation and solid propellant. We made heat flux measurements of the electrothermal plasma jet impinging on a sensor mimicking a disk of propellant. We made planar laser-induced fluorescence images of NO, a JA2 decomposition product, at the propellant surface. High speed video imaging of the propellant surface and scattering of ejected particles was used to study how the propellant surface evolves during exposure to plasma radiation. During the radiation interaction scattering particles and NO appeared between 100 and 150 microseconds after the beginning of the discharge and propagated away from the propellant surface. The ejected material occurred in identifiable structures that are irregular in shape and distribution suggesting that ejection occurred at semi-discrete locations on the surface rather than uniformly. During the plasma firing the propellant surface changed markedly by forming irregularly shaped decomposition structures that grew in size over the course of the discharge. No correlation was observed between the structure of the ejected material and the decomposition structures formed on the propellant surface during the discharge. After the plasma discharge, the propellant continued to react, with bubbles forming on the surface up to 9 ms after the discharge finished.

List of papers submitted or published that acknowledge ARO support during this reporting period. List the papers, including journal references, in the following categories:

(a) Papers published in peer-reviewed journals (N/A for none)

Number of Papers published in peer-reviewed journals: 0.00

(b) Papers published in non-peer-reviewed journals or in conference proceedings (N/A for none)

Number of Papers published in non peer-reviewed journals: 0.00

(c) Presentations

Number of Presentations: 0.00

Non Peer-Reviewed Conference Proceeding publications (other than abstracts):

Number of Non Peer-Reviewed Conference Proceeding publications (other than abstracts):   0

Peer-Reviewed Conference Proceeding publications (other than abstracts):

Number of Peer-Reviewed Conference Proceeding publications (other than abstracts):   0

(d) Manuscripts

Number of Manuscripts: 0.00

Number of Inventions:

Graduate Students

NAME	PERCENT SUPPORTED
Augustin Valdivia	0.17
Justin Wagner	0.17
FTE Equivalent:	**0.34**
Total Number:	**2**

Names of Post Doctorates

NAME	PERCENT_SUPPORTED
FTE Equivalent:	
Total Number:	

Names of Faculty Supported

NAME	PERCENT_SUPPORTED
FTE Equivalent:	
Total Number:	

Names of Under Graduate students supported

NAME	PERCENT_SUPPORTED
FTE Equivalent:	
Total Number:	

Student Metrics
This section only applies to graduating undergraduates supported by this agreement in this reporting period

The number of undergraduates funded by this agreement who graduated during this period: 0.00

The number of undergraduates funded by this agreement who graduated during this period with a degree in science, mathematics, engineering, or technology fields:...... 0.00

The number of undergraduates funded by your agreement who graduated during this period and will continue to pursue a graduate or Ph.D. degree in science, mathematics, engineering, or technology fields:...... 0.00

Number of graduating undergraduates who achieved a 3.5 GPA to 4.0 (4.0 max scale):...... 0.00

Number of graduating undergraduates funded by a DoD funded Center of Excellence grant for Education, Research and Engineering:...... 0.00

The number of undergraduates funded by your agreement who graduated during this period and intend to work for the Department of Defense 0.00

The number of undergraduates funded by your agreement who graduated during this period and will receive scholarships or fellowships for further studies in science, mathematics, engineering or technology fields:...... 0.00

Names of Personnel receiving masters degrees

NAME
Total Number:

Names of personnel receiving PHDs

NAME
Michael Ryan
Total Number: **1**

Names of other research staff

NAME	PERCENT_SUPPORTED
FTE Equivalent:	
Total Number:	

Sub Contractors (DD882)

Inventions (DD882)

Names of other research staff

NAME	PERCENT_SUPPORTED
FTE Equivalent:	
Total Number:	

Table of Contents

List of Appendixes and Illustrations

List of Appendixes

List of Illustrations

Statement of the Problem Studied

The objective of this work was to explore the mechanisms responsible for the observed benefits of electrothermal (ET) gun ignition, as well as reveal more information on possible burn rate enhancement of the propellant. The propellant used in all the experiments was 2.5 mm thick sheet JA2.

Because the plasma jet did not ignite the propellant in open air, a pressure chamber was constructed to create the confinement necessary for the propellant to ignite. Optical access was designed into the pressure chamber to conduct the same optical diagnostics originally intended for the open air interaction. With the original design version of the chamber, the propellant did not ignite until about 50 ms, well after the plasma discharge. In addition, it was discovered that a condensed aerosol formed as the plasma cooled, probably from vaporized metal and carbon in the plasma. This aerosol made the chamber optically thick directly following the plasma discharge. Lasers were completely attenuated as they passed through the chamber. Many modifications were made to the design to find some time period during the discharge during which laser diagnostics might be conducted, but they were not successful.

The studies of the interaction of JA2 propellant with plasma radiation alone were motivated by the importance of this interaction in the plasma ignition process. It was desired to conduct real-time measurements during the plasma propellant interaction. In these plasma radiation interaction experiments the propellant surface is separated from the plasma by a fused silica window and the plasma never touches the propellant. Broadband plasma radiation propagates through the window and causes decomposition reactions in the propellant, but the propellant does not ignite. Letting only the plasma radiation affect the propellant eliminated the problems with large background plasma luminosity and attenuation of laser interrogation beams and signal due to condensation. This enabled optical diagnostics which are the only practical means to obtain real-time measurements during the interaction. Further, the observed decrease in ignition delay and ignition delay jitter described earlier and for the desired increased burning rate in the propellant during a gun firing could be caused by the effects of plasma radiation on the propellant. Thus, the study of the plasma radiation interaction with solid propellant is very important to understanding and optimizing the benefits of the ETC gun.

Plasma radiation has been shown to cause blisters and subsurface voids throughout transparent JA2 samples 4 mm thick (Kappen and Beyer 2003), presumably due to gas generation from propellant decomposition. In the semi-transparent JA2 used for these experiments, with 0.05% graphite, blisters have been observed only at a depth less than 0.5 mm. In addition to the surface effects, significant gasification has been observed in plasma radiation-propellant interactions. Increased initial gasification during plasma ignition of propellant has been proposed as a cause for the decreased ignition delay and delay jitter (Beyer and Pesce-Rodriguez 2004). Also, modeling shows that the increased surface area due to subsurface void formation increases propellant burning rate (Koleczko, et al. 2001).

The experiments described here were designed to create time and spatially resolved observations of the plasma radiation-propellant interaction (PRPI) over the course of the plasma firing. Both radiative and conductive heat flux to a surface mimicking propellant were measured in an open air plasma jet. This gave some idea of the energy transport to the propellant surface in the PRPI studied later. In the PRPI experiments the plasma jet was confined to a chamber, separated from a disk of propellant by a fused silica window. Transport of decomposition products from the propellant surface was observed to give some information on the reactions taking place at the surface of the propellant as well as fluid flow at the propellant surface during a precursor step to

radiative ignition. An intensified CCD camera was used to image nitric oxide (NO) by planar laser induced fluorescence and particulates by planar laser Mie scattering (PLMS). In addition, high speed video of the propellant surface was taken during the radiation-propellant interaction simultaneously with PLMS imaging away from the surface. This was designed to observe the propellant surface as it decomposed as well as correlate reaction products with what was observed on the propellant surface.

<div align="center">**Summary of Important Results**</div>

The experimental set-ups used to obtain the results below are described briefly in the Appendix.

PLASMA RADIATION

Figure 1 shows the plasma radiation intensity measured by a fast response photodiode. The photodiode was placed 11.4 cm above the plasma chamber window, with a neutral density filter (OD 2) attenuating the plasma light. The intensity ramps up rapidly and peaks at about 80 µs. The radiation then steadily decreases until between 600-650 µs, when the capacitor stops discharging. The intensity decays exponentially from 600 µs to 1500 µs. The dip in intensity around 300 µs is probably a result of the capillary voltage switching polarity as the capacitor current oscillates. After the firing the acrylic window guard is always somewhat blackened and the surface looks like it was partially melted from the plasma. The fused silica mask always has much more deposition on the surface than the acrylic mask and is opaque after firing. The acrylic mask is transparent after the firing. Greater ablation from the acrylic surface might explain the difference in the two surfaces after firing. The steady intensity decay during the discharge might be explained by the effect of the plasma on the mask. No direct measurements of heat flux to the propellant surface were made, but for an order of magnitude estimate it can be assumed the confined plasma produces fluxes equal to or higher than the same plasma expanding into open air. A measurement was made of the peak radiative flux on a probe 4.67 cm from the jet exit of a plasma expanding into room air to be 2500 W/cm^2 and the flux was above 1000 W/cm^2 for the entire capacitor discharge.
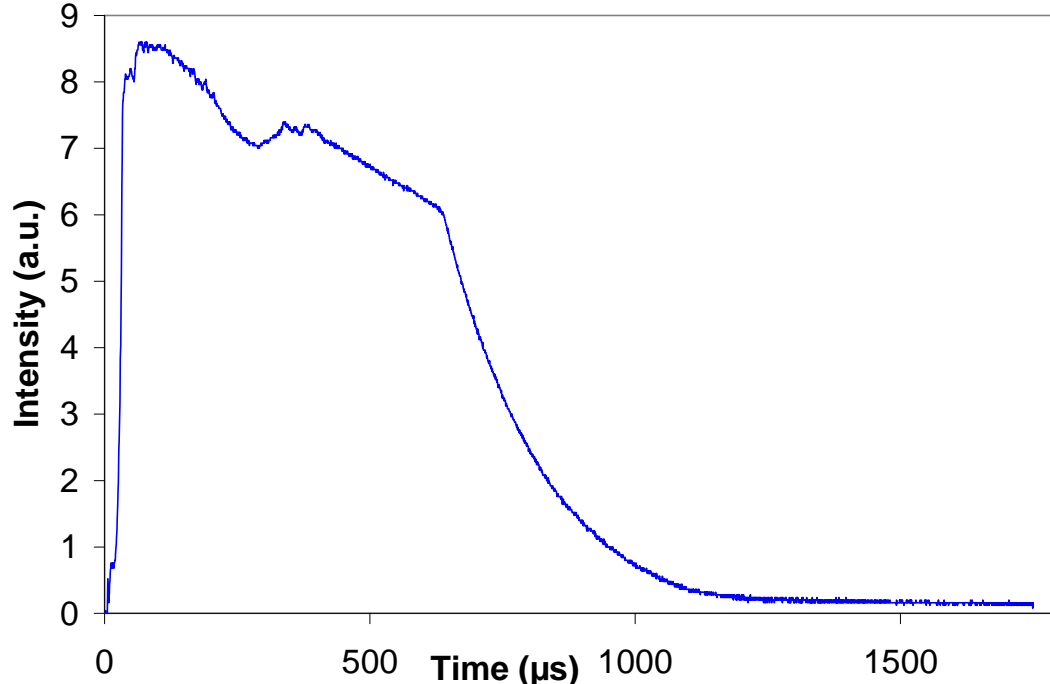

Figure 1: Plasma radiation intensity measured by a fast response photodiode

Plasma spectra combined from a number of firings with the acrylic mask can be seen in Fig. 2. The spectral range of the spectrometer is 120 nm so each curve is a combination of four

acquisitions at the same delay. Curves were produced for 150 µs and 500 µs delays. At both delays the spectrum is characterized by broadband emission with a few noticeable absorption lines or bands at 428, 470 and 520 nm. This is characteristic of a confined electrothermal plasma discharge. The cutoff below 380 nm is due to attenuation by acrylic. The oscillations on the right side of both curves are due to interference fringes on the detector.
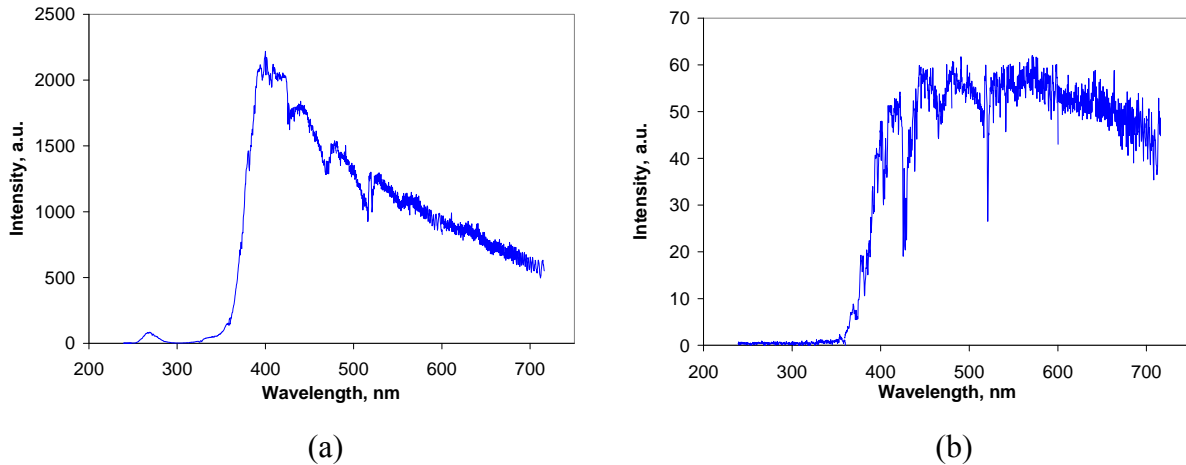

(a)   (b)

Figure 2: Plasma emission spectra at (a) 150 µs, and (b) 500 µs

The integrated emission intensity at 500 µs is much less than that at 150 µs and the spectra change over time. The reduction in intensity is probably a combination of lower energy in the plasma and higher attenuation through the mask as the surface is degraded. At 150 µs there is a marked peak at 400 nm. Because the acrylic cuts off at 380 nm, it is impossible to know where the true plasma radiation peak is and the peak is probably at a lower wavelength than observed. At 500 µs the peak shifted to between 500-600 nm. This indicates a reduction in temperature of the plasma between 150 to 500 µs.

Before these radiation experiments began there was some question as to how much the plasma radiation would affect the propellant, and also how similar the effects would be to results from other studies that focus on interactions of plasma with graphite free JA2 propellant (Beyer and Pesce-Rodriguez 2004, Koleczko, et al. 2001). Most tests involving plasma propellant interactions involve higher plasma energies than the 3.1 kJ of the current plasma. In addition, graphite free JA2 transmits more radiation in depth than the propellant used in these experiments. Figure 3 shows propellant discs before and after exposure to plasma radiation and an open air plasma jet. The level of interaction from plasma radiation, while not as great as that from an open air plasma jet, and far from ignition, is enough to have clear visible effects on the surface of the JA2 disc.

The structures produced on the propellant surface from plasma radiation exposure can be better seen in the higher resolution monochrome image shown in Fig. 4. These structures are caused by decomposition reactions taking place in the propellant as a result of plasma radiation. The brighter regions correspond to blisters and in-depth voids formed in the semi-transparent JA2 after exposure to plasma radiation. Kappen and Beyer (2003) published surface images as well as cross sectional images of transparent JA2 after exposure to plasma radiation. Kappen and Beyer's images showed in depth voids in the propellant material that corresponded to the circular structures seen on the surface images. This is the reason these structures are termed "blisters." The ranges of sizes of the structures observed on transparent and semi-transparent propellant are very similar. There is smaller structure in individual blisters on the semi-transparent JA2, while

this is not observed in the transparent JA2. The major structures seen at the propellant surface are discrete objects, circular in shape, with a maximum diameter between 1-2 mm. In semi-transparent JA2 used in the current study they were observed to a depth less than 0.5 mm, while in transparent JA2 they were observed throughout the propellant sample (Kappen and Beyer 2003). The similar size and shape of the structures in transparent and semi-transparent JA2 implies that decomposition from graphite heating is probably not a major cause for the surface changes observed.
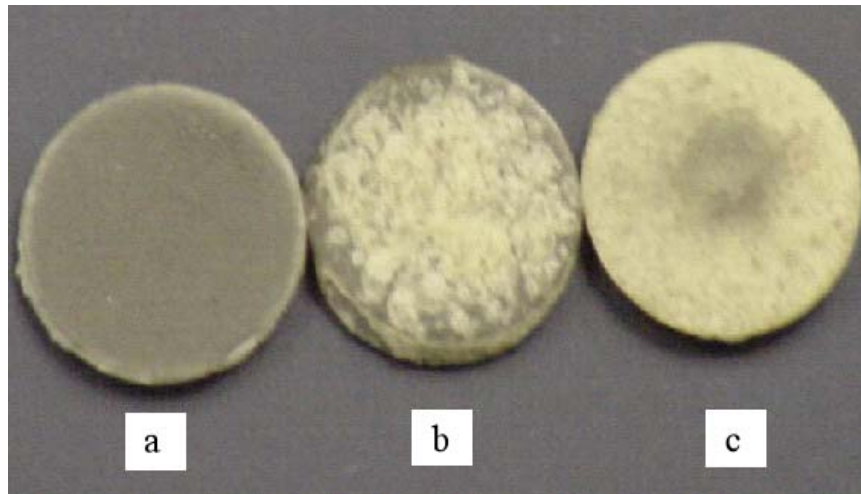
Figure 3: JA2 disc surface a) before, b) after plasma radiation exposure, and c) after open air plasma jet impingement
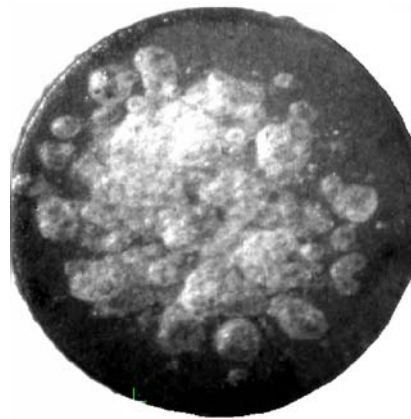
Figure 4: Semi-transparent JA2 propellant surface after exposure to plasma radiation during current study

NITRIC OXIDE PLIF

An example NO PLIF image is shown with a diagram of the experimental geometry in Fig. 5. The brightest swath at the top of the image is propellant luminosity/radiation scattering. Radiation from the plasma travels from bottom to top. The laser propagates from left to right across the image. The entire propellant disk is seen in the camera's field of view.
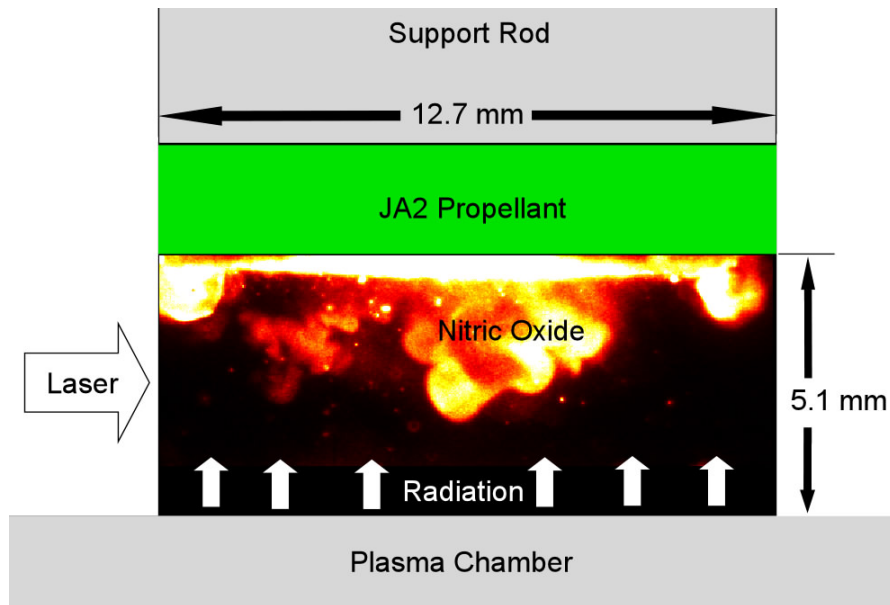
Figure 5: Geometry for camera field of view in NO PLIF and YAG PLMS experiments

A series of example NO PLIF images, one taken from each delay sampled (out of 3 images per delay), can be seen in Fig. 6. They are arranged such that a representative time history is shown. Each image is false colored from grayscale and has been rescaled individually in order to better visualize the NO. Many of the images show scattering off large particles as well as bright structures related to the disc edge in addition to the structures containing NO below the center of the propellant. To distinguish between NO fluorescence and scattering, a few images were taken with the pump laser tuned slightly off resonance. An example image at 500 μs delay can be seen in Fig. 7. This image's intensity was scaled such that signal of the same intensity as the minimum brightness structures in the NO PLIF images would clearly be visible. The large particles can still be seen in Fig. 7 as well as some possible scattering very close to the propellant surface. However, the large structures away from the propellant surface and at the edge are observed only when the laser is tuned on resonance.

NO signal is not observed until after 100 μs in Fig. 6. At 150 μs small globular structures appear and grow as the discharge progresses. These are labeled in Fig. 6. In many of the images, especially at times after 350 μs, discrete nitric oxide structures can be seen separate from the propellant surface. This suggests that NO is being produced in short bursts rather than continuous jets during the discharge. An alternative explanation is that the clouds of NO propagate parallel to the surface of the propellant. However, very few structures in the images have a cross section consistent with NO moving sideways, so this is not as likely. From the unprocessed images it can be inferred that the brightest NO signal is present when the clouds first appear at 150 μs, and the signal gradually decreases until 300 μs where it stays relatively constant. The temperatures of the propellant surface and the gases being released by the propellant during the interaction were not measured. Simulated spectra suggest that the NO signal should increase with decreasing temperature. It is reasonable to assume that the gases ejected from the propellant are at temperatures equal to or greater than the surrounding air as a result of the energy deposition by the plasma radiation. If the temperature of the gases produced was greater than the ambient air, the temperature would decrease as the gases propagated away from the propellant and mixed with ambient air. Nitric Oxide does not absorb in the visible range and so plasma light would not affect it. The resulting NO PLIF signal would increase from this temperature decrease. Because the signal is observed to decrease as the NO structures propagate

away from the propellant, the other main driver of fluorescence signal, species number density, must be the cause. This matches expectations of the NO structures mixing with and diffusing into the ambient air.
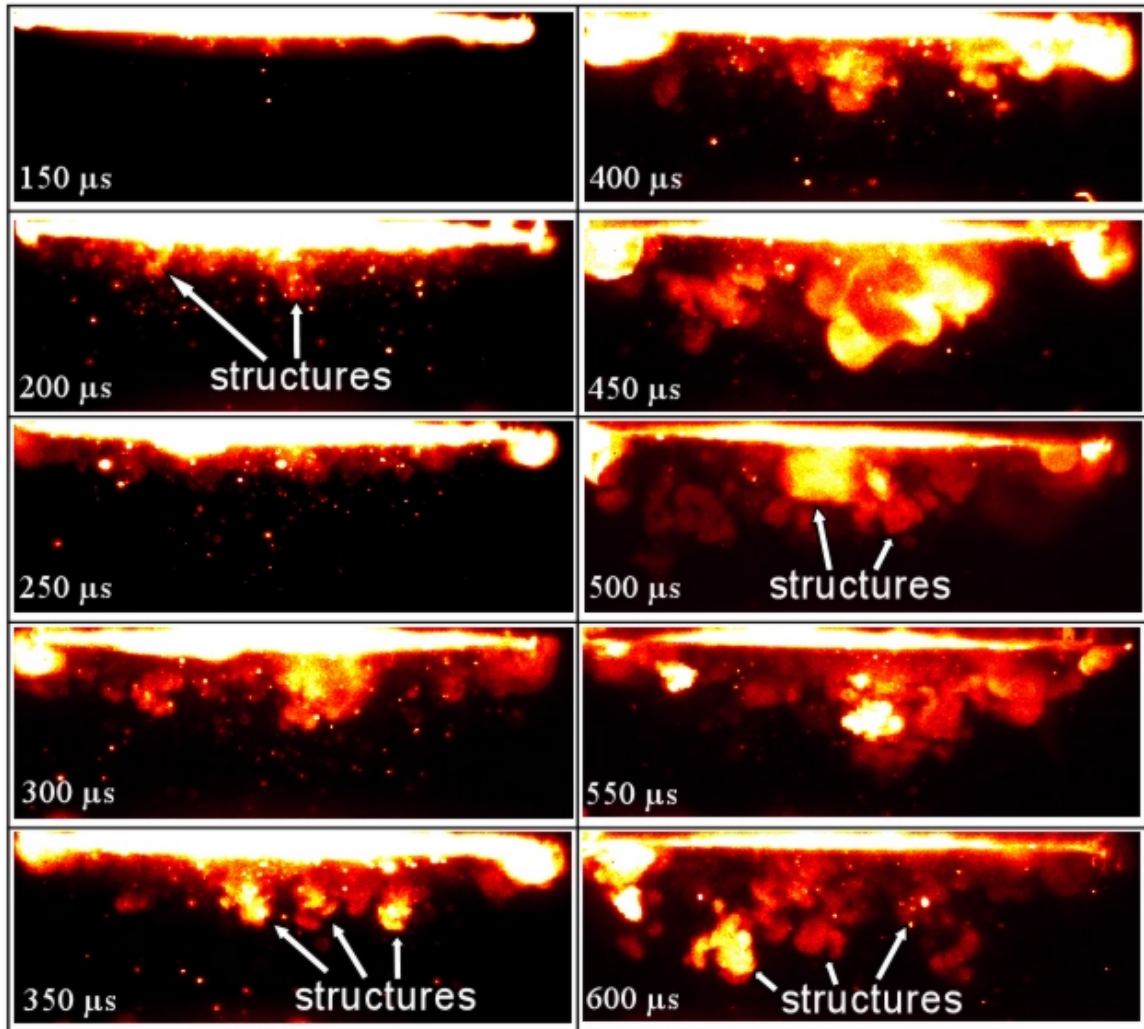
Figure 6: Time sequence of NO PLIF images created from separate firings. NO ejection structures are labeled
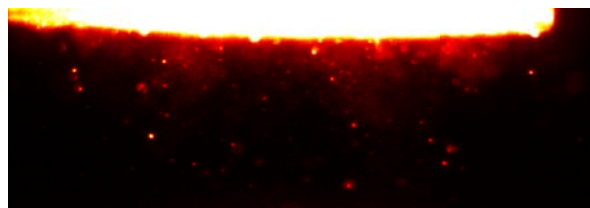
Figure 7: Example image of tuning NO pump laser off absorption line at 500 μs delay

The velocity of the NO structures was roughly estimated by measuring the average rate of change of the distance from the bottom edge of the NO structures to the propellant surface. The order of magnitude of the velocity calculated is 10 m/s. It is unclear whether the source of this ejected material is the outer surface or pockets of decomposition directly underneath the surface.

The pressure difference needed for isentropic expansion in air to cause this velocity is a small fraction of atmospheric pressure. While double base propellant decomposition can be pressure dependent due to autocatalysis from NO_2 (Kimura 1988), pressure differences in these experiments are probably small enough that they do not affect decomposition rate, which would affect burn rate in a gun firing.

LASER MIE SCATTERING

Figure 8 shows laser scattering images taken with the pulsed double Nd:YAG of particles emitted from the propellant. These were individually rescaled from grayscale images. A representative time history similar to Fig. 6 gives an idea of the type of scattering structures and how they propagate during the discharge.
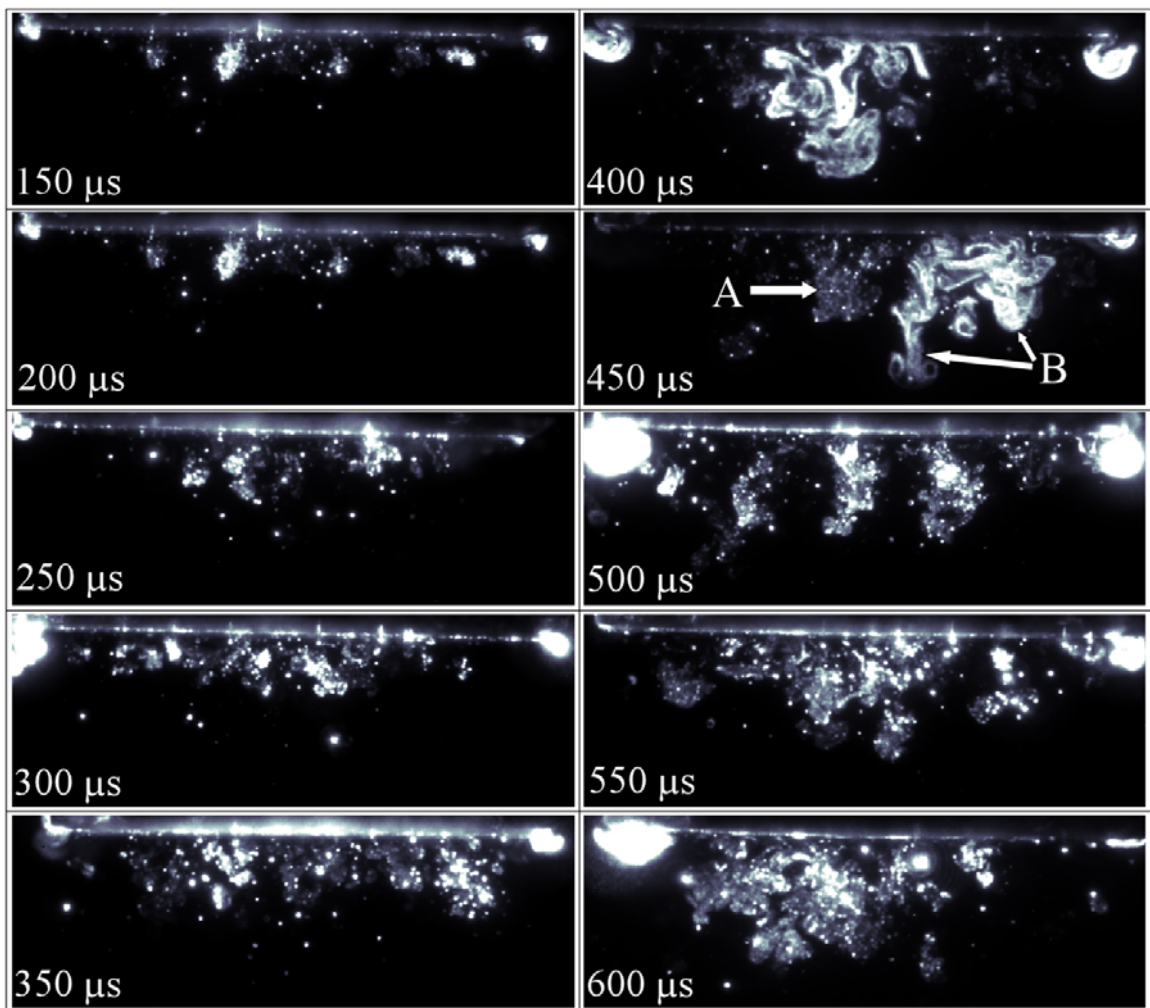
Figure 8: Time sequence of laser scattering composed of images from individual runs. Labels A and B mark smaller more common scattering structures and larger, brighter, less common scattering structures respectively.

Once again the structures begin to appear at 150 µs and grow larger and propagate down as the discharge progresses. There are two distinct types of scattering structures observed. The first, composed of a range of particle sizes, appear and grow as the large majority of NO clouds do in

Fig. 6. This is labeled "A" in the 450 μs image of Fig. 6. The shapes are similar enough that they probably are the same type of structures, visualized two different ways. The second type of structure, seen only in the 400 and 450 μs images away from the propellant, but also throughout the images at the propellant edges, is characterized by much brighter scattering, larger size, and homogeneity of the particle sizes, inferred from the relatively constant signal throughout the structure. This is labeled "B" in the 450 μs image of Fig. 6. This structure type is much rarer, as it was only seen away from the propellant surface on those two images in 25 runs. However, the surface of the propellant after these two runs looked no different to the naked eye than after any other run. A corresponding NO structure might be seen in the 450 μs image of Fig. 6. The large NO structure in the center of that image is brighter than the surrounding structures, bigger, and has a much smoother surface. In addition, similar bright structures can be seen at the edges of the propellant in Fig. 6.

The two different structures observed can be seen side by side in the 450 μs image of Fig. 8. That image is scaled differently from the majority of images in the figure. The smaller structure, with the same brightness as the other blotchy structures in the other images, has intensity counts ranging from 5,000 to 20,000 while the larger structure has a brightness similar to the material coming off the edge of the propellant and saturates the detector with 65,535 counts at its brightest. The brighter structures correspond to an ejection where more material is produced. This is supported by the larger scattering signal and size of these structures. They might appear at the edges of the propellant because the grains are exposed there. During these radiation interactions it has been observed that the blisters form along the propellant grain. In sheet JA2 propellant, the grain is parallel to the surface. Blisters that would normally be forming underneath the surface are exposed to open air there and so would be better able to discharge material. In the 450 μs image of Fig. 8 a structure similar to a mushroom-like vortex ring can be seen at the bottom. This might correspond to a stronger than normal jet of material coming from the propellant surface.

The images show a large number of particles separating from the propellant surface during the radiation interaction. The particles have a range of sizes. The smallest particles, especially in the large bright structures, are unresolved, while the largest are around 6×6 pixels, corresponding to a diameter of 156 μm (individual pixels correspond to an area 26 by 26 μm). JA2 propellant has three major nitrate esters, two of which, nitroglycerin (NG) and diethylene glycol dinitrate (DEGDN), are liquid at room temperature. JA2 also has many other components at low concentration so it is impossible to know the composition of the particles in the images shown. They could be chunks of nitrocellulose (NC) fiber, liquid mists of NG or DEGDN, an agglomeration of NC, NG, and DEGDN, or some smaller decomposition product that scatters light. The large jump in pressurization seen in closed bomb plasma ignition tests (Lieb, et al. 2001) during the plasma discharge might be due in part to the increased burning surface area provided by these particles, in addition to the known outgassing that occurs. No film or buildup of particulates was ever observed on the top of the chamber. In addition, a scale with a 0.002 g resolution could detect no difference in the mass of the propellant disks before and after radiation exposure. Propellant disks normally had a mass around 0.5 g, and thus only less than 0.4% of the semi-transparent JA2 propellant mass is lost during this interaction with plasma radiation.

The structures observed jetting from the propellant could directly correspond to formation of individual blisters on the propellant surface. Blisters overlap on the propellant surface so in order to create clear individual jets they would probably need to form at different times.

9

SIMULTANEOUS TWO CAMERA IMAGING

Figure 9 shows a representative series of images of the propellant surface from a single run using an acrylic mask on the window. The framing rate of the camera was 50 kHz and the illumination source was the same plasma light that caused the decomposition. While the images were taken every 20 μs, they are displayed at intervals of 60 μs to conserve space.
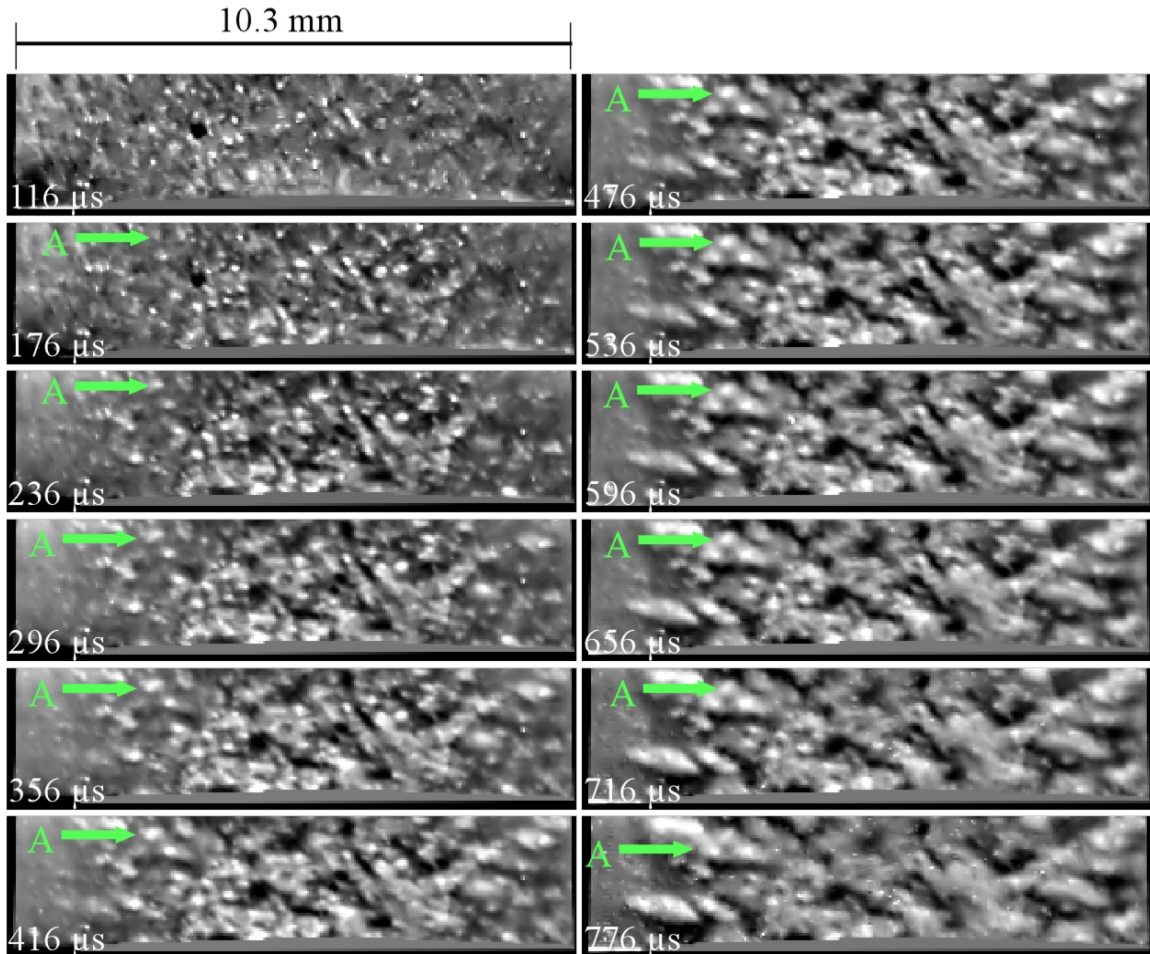
Figure 9: Time series of propellant surface during the plasma discharge during 2 camera experiment. Delay times from the capacitor trigger are marked in the bottom left corner of each image. The label A marks a structure as it changes throughout the plasma discharge.

For better viewing these images have been processed by a variety of methods using Matlab. All linear filtering was accomplished by modifying the two dimensional Fourier transforms of each image. These images have had their DC component filtered out to account for the change of the plasma brightness over time. Also, their low frequency components have been filtered out to account for spatial variations in the lighting. These spatial variations imply that the confined plasma has spatial structure inside the chamber. Camera fixed pattern noise has been filtered out as well. A code (Kovesi 1999) was run to reduce the readout noise and improve visualization of the affected areas of the propellant. Otherwise the images at the end of the sequence would be very difficult to see because the illuminating plasma light is reduced at that time. The images have been transformed to show the propellant surface as if viewed directly from below. Further, the images were intensity scaled so that the brightest 1% appeared white and the darkest 1%

appeared black. A section on the bottom of each image was deleted because it was completely saturated over most of the run. This was a result of bleeding from oversaturated pixels that imaged the plasma chamber window beyond the edge of the mirror.

In general, the brighter regions of the images are the areas that have been affected by the plasma radiation. This is reasonable since the blisters seen by the naked eye are white while the unaffected surface is dark green. Visible propellant scattering spectra displayed earlier show that the blister reflectance is much higher than that of the pristine surface. However, at the beginning of the sequence preexisting blemishes on the surface appear as bright spots. Most of these blemishes diminish and disappear as the propellant begins to change. Some coincide with spots where blisters begin to form on the surface.

The propellant surface begins to change at about 116 μs, which is the first image in the sequence. This coincides with the ICCD camera experiments where material began ejecting from the propellant between 100 and 150 μs. The surface changes throughout the plasma discharge, and continues to change afterwards albeit at a much lower rate. During the discharge, changes in the surface are visible between consecutive images 20 μs apart. Irregularly shaped small structures are observed to appear and grow through random expansion at their edges and merge with other growing structures. An example of this is labeled "A" in Fig. 9. Blisters might not be the correct term to describe these structures because there is no obvious evidence of gas forming beneath the surface. These structures might just be discoloration of the top layer of propellant as it decomposes. Also, they are smaller than the 1 mm diameter circular blisters seen in Fig. 4, as well as irregular in shape. The surface changes earlier and more quickly at the center of the image, which is closer to the center of the propellant disk, and then later nearer the edges. This is expected because the irradiation at the propellant disk decreases with increasing distance away from the center. Most structures start off very small, with a characteristic size in the range of 0.1 mm, and by 776 μs grow to a size around 0.5 mm. Most large structures at the end of the firing are an agglomeration of smaller ones. They are not isolated but connected to the other large structures, and show considerable variation scattering intensity over their area, evidence of their formation history. A structure the size of the large blisters in Fig. 4 was never observed in any of the runs by the propellant surface camera. It will be shown later that the propellant continues to change well after the capacitor is finished discharging and that the larger blisters observed after the firing might be a result of this.

An example of the propellant surface image ratio technique is shown in Fig. 10. The ratio image has many small blobs of varied shape and size. These regions of change support the conclusion that the structures seen on the propellant surface grow randomly by small amounts between consecutive images during the plasma discharge. Although there are regions of change that encompass all of a smaller decomposition structure (labeled "A" in Fig. 10), in general these ratio regions comprise a small part of an existing structure or are on some portion of the edge of an existing structure (labeled "B" in Fig. 10).

Statistics on these regions can be compiled by applying this ratio method to multiple runs. The ratio images are converted to binary images and the regions of change are defined as regions of pixels that are 4-connected, meaning neighboring pixels to the left, right, top and bottom that are above the threshold are part of the same region. Diagonally connected pixels are not necessarily part of the same region. Data such as the number of regions, total area covered, and median size can be computed. The data are averaged over three runs for each mask, and a 95% confidence interval is computed using a student's *t*-distribution estimation. These data show some interesting trends.
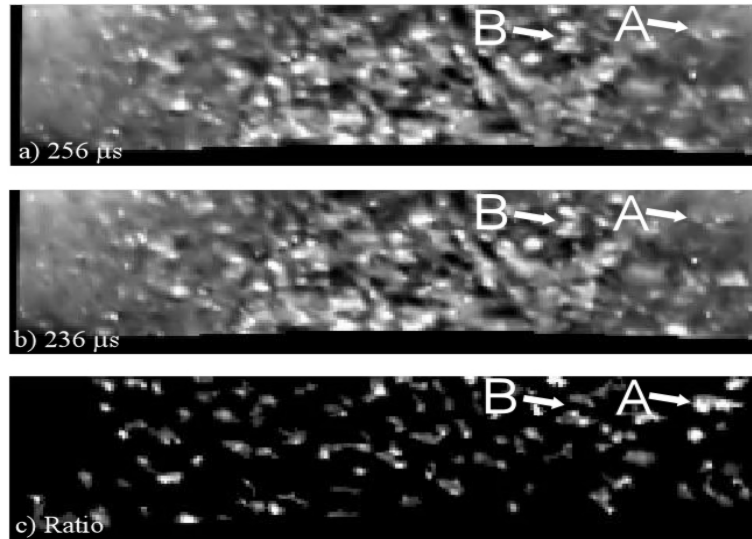
Figure 10: Example of difference image, with the two images used to calculate it.

Figure 11 shows the average intensity per pixel of unprocessed propellant surface images over the course of several runs using both acrylic and fused silica window masks. This shows the timing for the plasma illumination. While there is some variation, on the whole it resembles the radiation intensity history of Fig. 1. The intensities with both masks are expected to be the same because the camera filters block the UV light. The maximum illumination is reached shortly after 100 μs. There is a local minimum at about 300 μs when the current oscillates in the discharge circuit, and a secondary maximum is reached at about 400 μs, after which the signal tapers off.
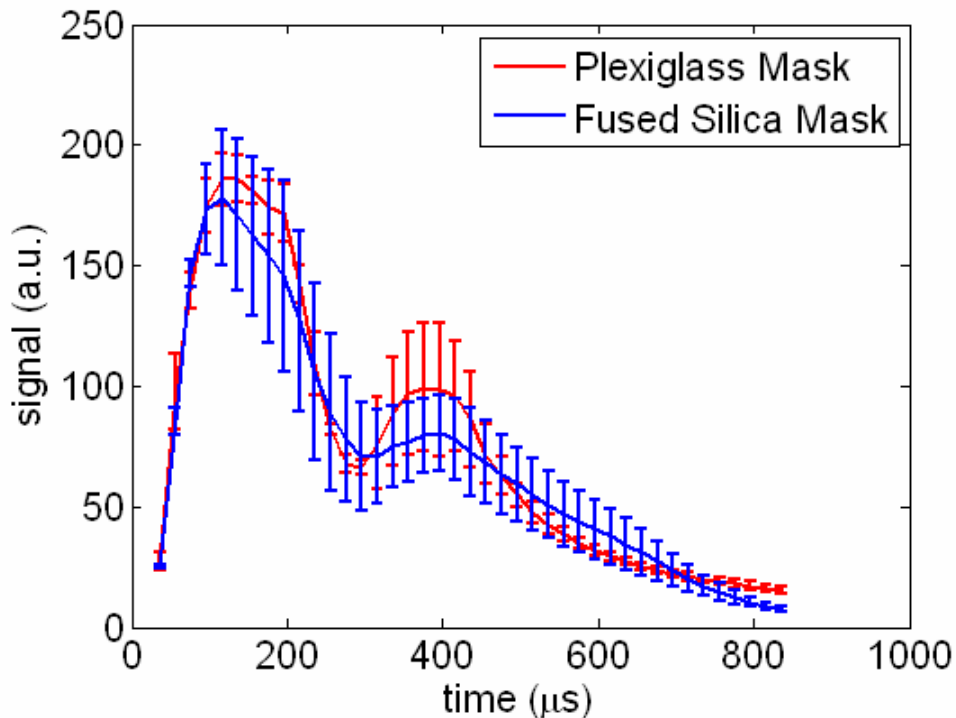
Figure 11: Average intensity of propellant surface image using each window mask.

Figure 12 shows the number of regions of change over the course of several runs. There is no major noticeable difference between the runs using a fused silica mask and an acrylic mask.

Also, the number of regions peaks shortly after 200 µs. This is 100 µs after the peak of illumination from the plasma. After the peak the number of regions steadily declines until 600 µs at which point the number of regions increases slightly or stays constant. The data after 600 µs are unreliable because the signal to noise ratio of the propellant images is very low at this point. In addition, as mentioned before, the data before 100 µs are also suspect because of the very rapid changes in illumination over that short time period. The number of regions of change begins at a finite value and then decreases until 100 µs. This data has been ignored. Viewing the propellant surface images by eye shows that this is not actually happening.
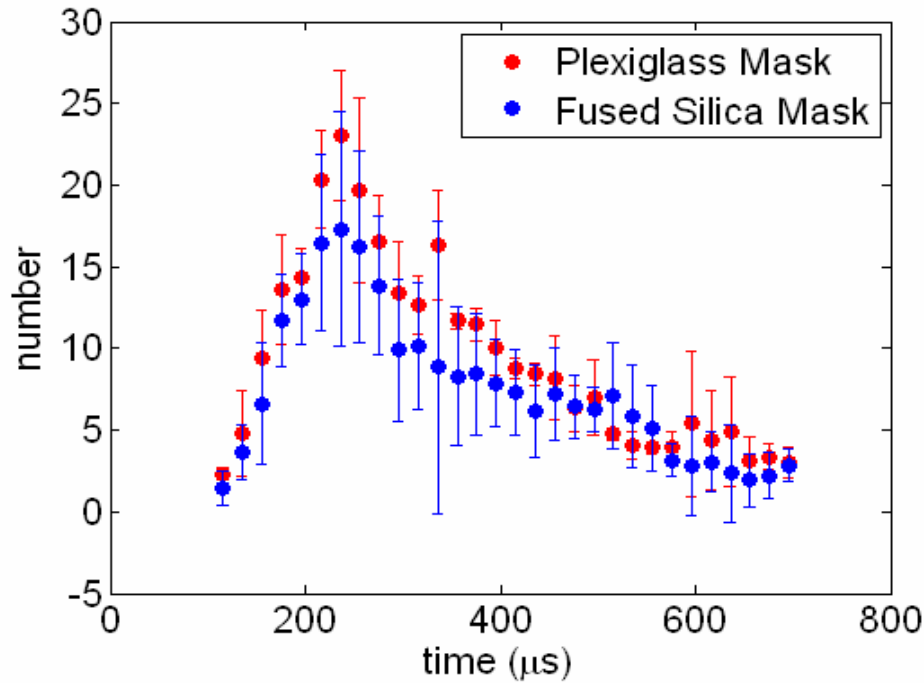

Figure 12: Average number of regions of change appearing over multiple runs.

Figure 13 shows the percent of total area of each ratio image covered by regions of change. The data were generated by summing the area covered by all regions of change and comparing it to the size of the image. Figure 14 shows the median size in pixels of the regions of change. Both figures show data for the same runs shown in Fig 12. Median region size was chosen instead of average region size to avoid the skewing of data due to the presence of artificially large regions of change at the edge of the image as previously mentioned. While these graphs display different statistics, they show the same trends as Fig. 12. Both total area and median area of regions of change reach a peak at about 200 µs, although the large variation between individual runs in Fig. 14 causes the confidence interval to be large. On the whole, both total area and median area show gradual declines after the initial peaks. The analysis results are unreliable before 100 µs and after 600 µs as explained earlier.

The fact that the data trends are consistent over the runs for all these statistical quantities gives greater credibility to the trends discovered by this ratio method. Blocking the UV plasma light from reaching the propellant has no observable effect on the propellant decomposition. The ratio structures form at the same rate, at the same sizes, and in the same numbers between runs with an acrylic and a fused silica window mask. The same fused silica run shows lower illumination in Fig. 11, lower number of regions in Fig. 12, and lower percent area in Fig. 13. The window cracked during this run and the lower amount of plasma radiation reaching the propellant

13

resulted in less energy transfer to the propellant and hence less decomposition at the surface. From this result, we can conclude that the difference in radiative energy reaching the propellant surface between using the fused silica mask and the acrylic mask is insignificant, and the additional UV light hitting the propellant through the fused silica mask has no observable effect over the visible/IR plasma light. This supports the conclusion that the interaction between the plasma radiation and the propellant is largely a thermal decomposition process.
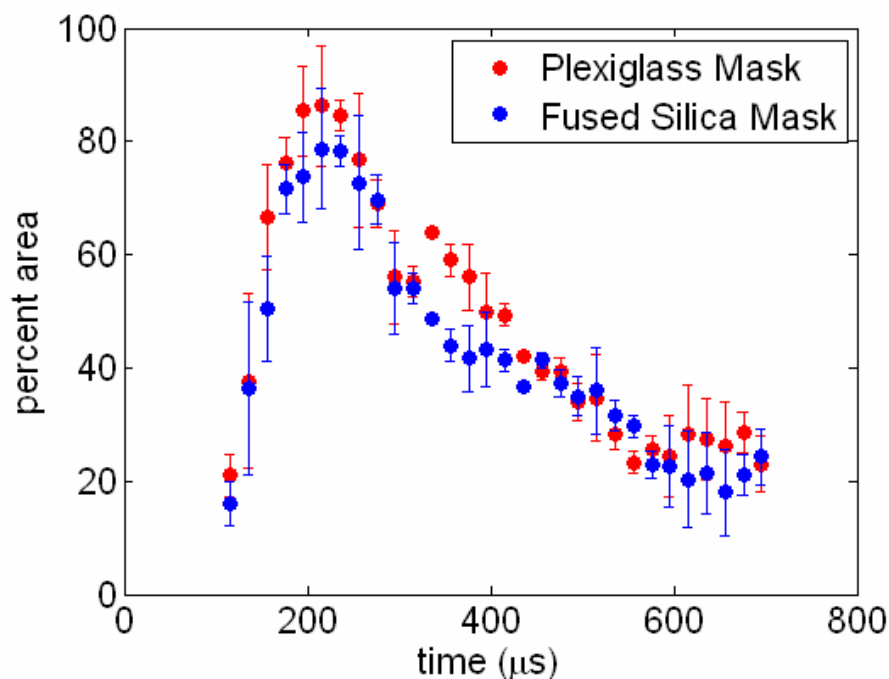

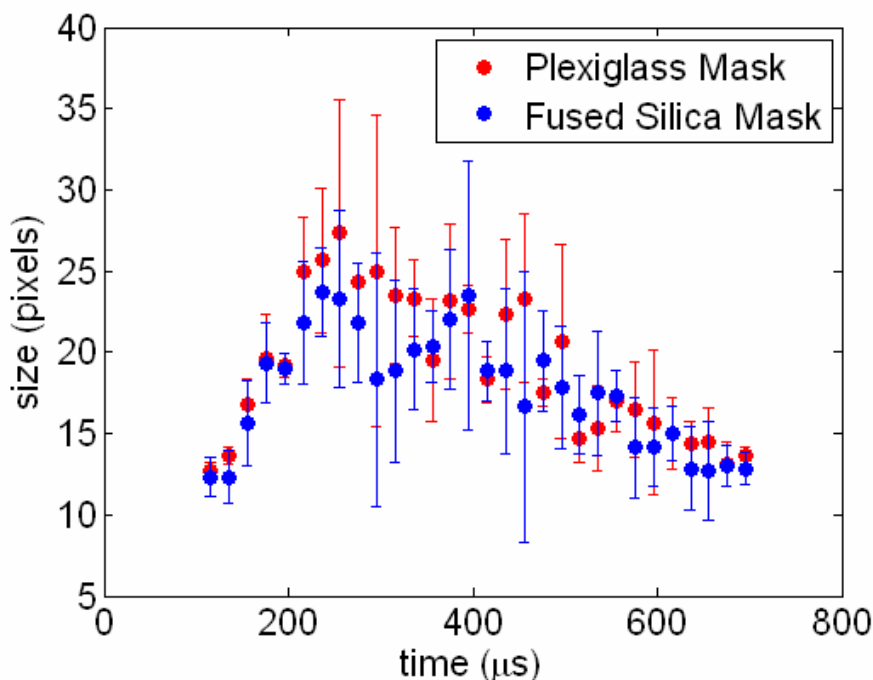Figure 13: Average percent of total image area covered by regions of change for each mask.

Figure 14: Average median size of regions of change over multiple runs.

14

One last observation made using the propellant surface images alone is shown in Figure 15. The last image illuminated by the plasma during a run (836 μs) is compared with an image of the same propellant surface a few minutes after the run. The propellant surface has changed significantly during this interval. There are no large blisters evident in the image after firing. This is surprising because Fig. 4, a larger and lower resolution view of a similar surface shows larger blisters. However, the larger blisters are difficult to distinguish in the center of the propellant in Fig. 4, which is the field of view for Fig. 15. The image of the propellant after the firing does show that the area containing decomposition structures is larger. Therefore the propellant continues to react and decompose after the plasma irradiation ceases.

(a)

(b)
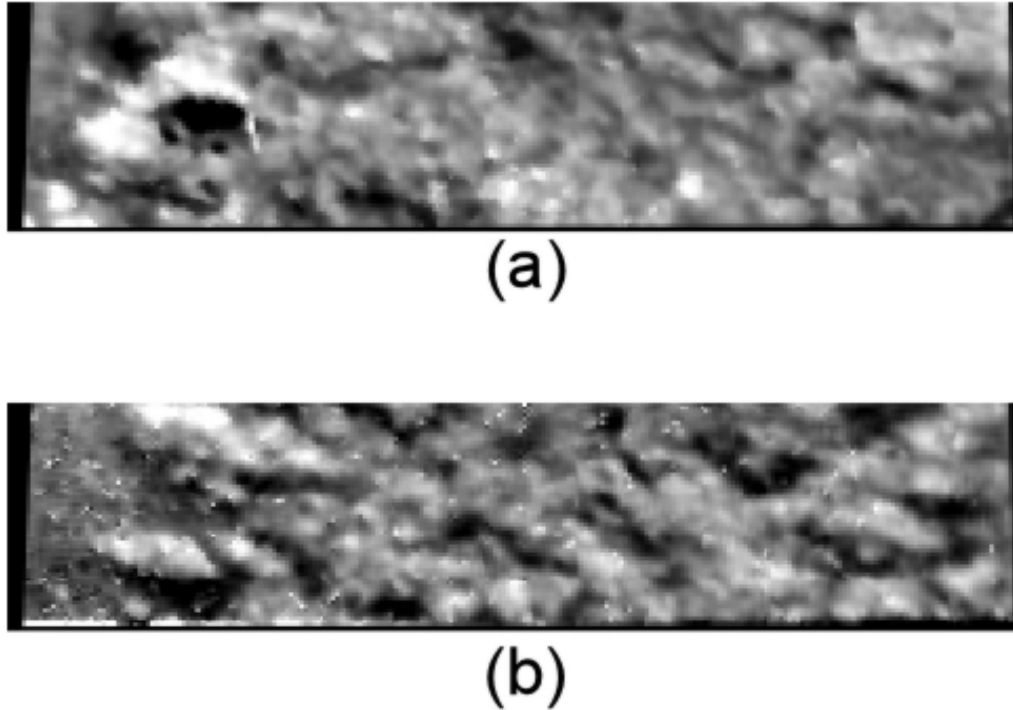
Figure 15: Comparison between propellant surface images at a delay of (a) 5 minutes after the plasma firing   (b) 836 μs

Figure 16 is an example time sequence of laser scattering images all taken during the same run. The sequence very closely resembles the pseudo time series taken by the ICCD in Fig. 8. The major differences are that there is lower resolution and a smaller field of view for the images in Fig. 16. Also, the exposure time of the camera is greatly increased so the background plasma light can be seen scattering off particles outside the focal plane at delays of 136 and 236 μs. One of the original reasons for using the high framing rate cameras was to observe how the material propagated away from the propellant surface during the discharge. The sequence in Fig. 16 starts out the same as in Fig. 8, with particles appearing between 100 and 150 μs. Material propagates downward as the discharge progresses. However, the structures observed throughout Fig. 8 are not readily apparent over times of 136 to 536 μs in Fig. 16. It is probable that the particles in the laser plane are slightly obscured by scattering from plasma light. After 536 μs there is an obvious correlation between images, and the particle structures change very little from frame to frame. The bright structure that is fully formed at a delay of 536 μs is too bright to be obscured by plasma light scattering, and appears to form at about 200 μs. The temporal resolution of the image sequence is not high enough to resolve trajectories of individual particles and larger structures during the plasma discharge. It should also be noted that the momentum of the

structures observed must be very small for them to form in 200 µs and then be stopped by the surrounding air for the rest of the sequence.

Figure 17 is an example time series of cross-plane plots of both the scattering and propellant surface images. The observer is looking at both the laser scattering and propellant surface from a point below the propellant and towards the cameras. The propellant is reacting throughout the entire field of view of the camera during the entire series, yet the ejection structures are not appearing throughout the width of the scattering images. An examination of the particle evolution reveals no obvious correlation between the particles and the changes to the surface. While brighter particle structures do appear at decomposition regions, particle structures do not appear over all decomposition regions. Unfortunately the half width of the laser sheet, marked in the images, is larger than the size of most decomposition structures during the discharge. This makes it difficult to determine the exact location from where the propellant material is ejecting. After 536 µs the particles away from the propellant surface move very little between images, and so these later images would not be expected to correlate with what is observed on the propellant surface.
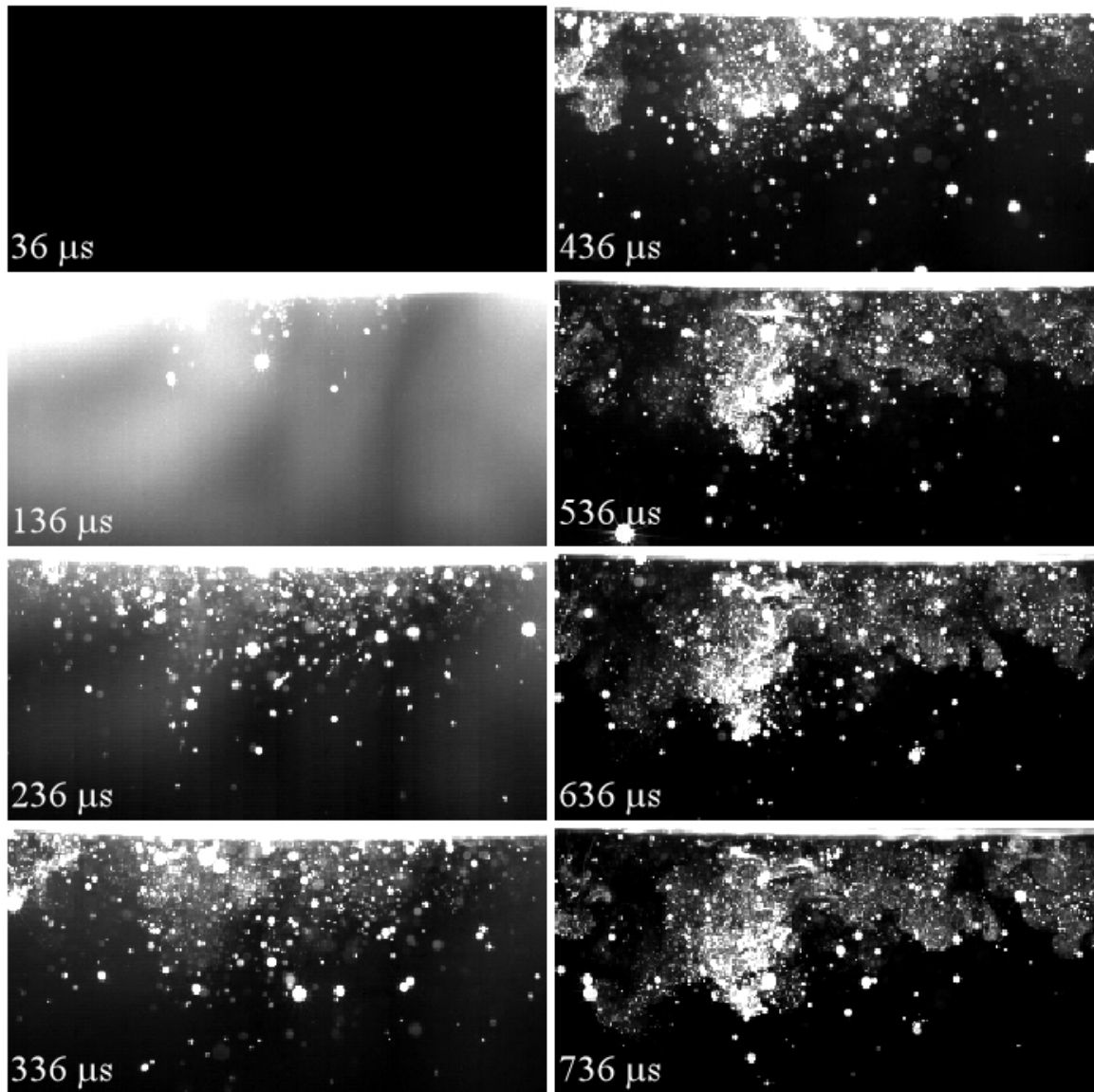
Figure 16: Example time sequence of laser scattering images taken during the same run.
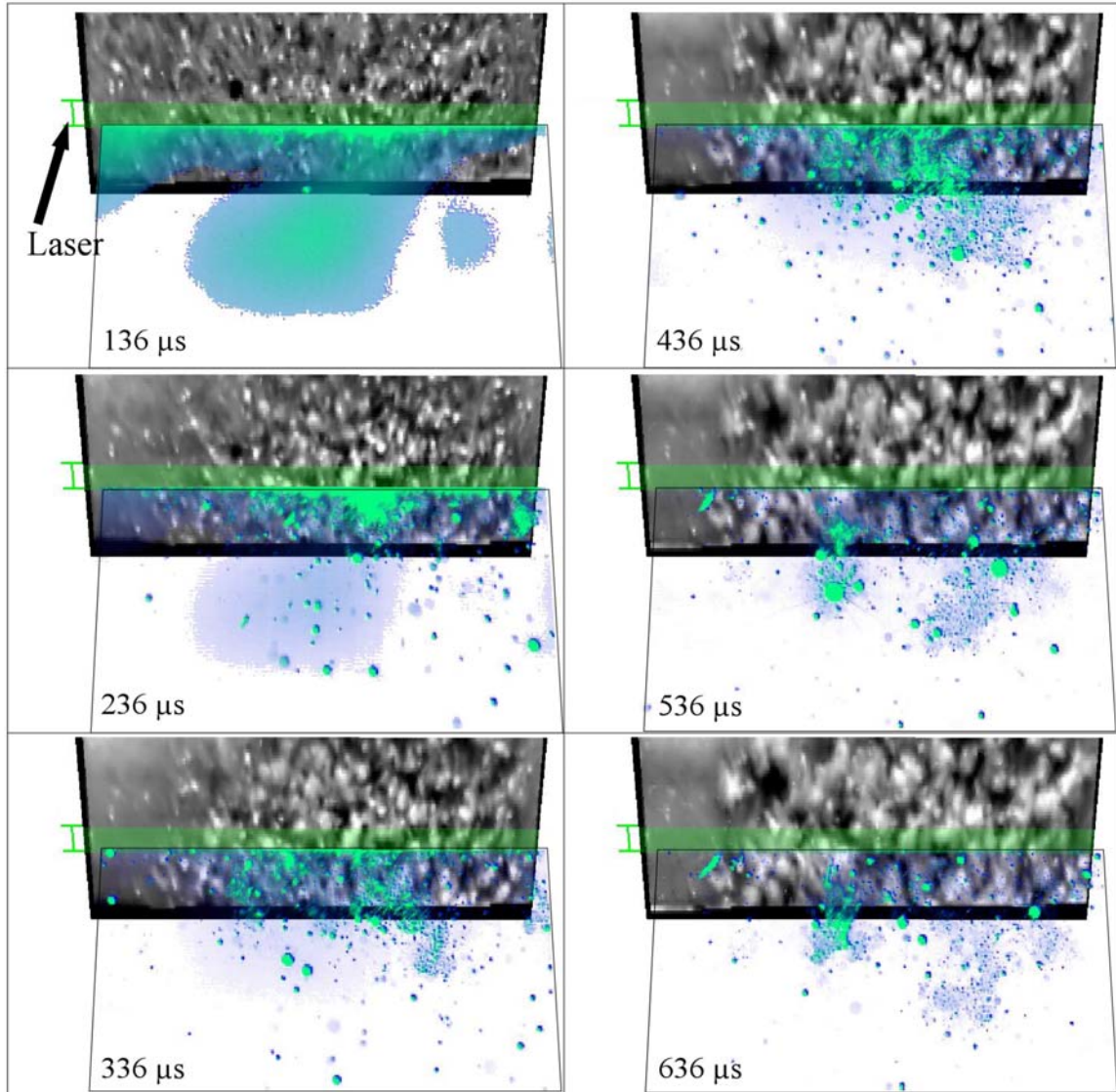
Figure 17: Example time series of propellant surface images and laser scattering images plotted together.

Attempts to correlate sections of the particle images away from the propellant surface with the region of propellant images encompassed by the laser met with little success. Figure 18 shows examples of correlations made from two runs at three different delays. Delays of 236 and 436 µs are during the plasma discharge while the delay of 636 µs is on the tail end of the discharge and is not expected to produce a strong correlation. The cross-correlations for each time delay were converted into an array so that the top row corresponds to the correlation of the scattering image strip closest to the propellant surface. Surface plots of the cross correlations were made and appear at the same viewing angle as the laser scattering images in Fig. 17. The top of each plot shows the correlation for the strip closest to the propellant surface, with the bottom being the furthest away. The run on the left is the same run that produced Fig. 17.
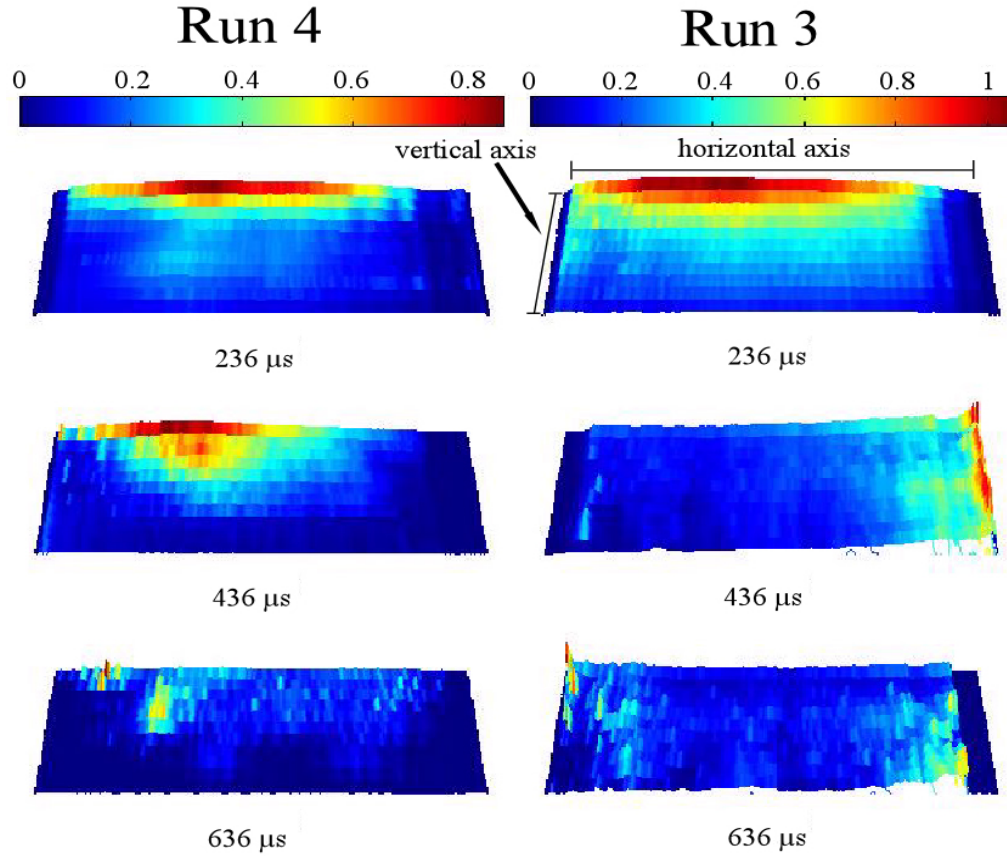
Figure 18: Example cross correlations between the propellant surface and laser scattering images.

If the scattering and surface images correlated well, a peak would be expected in the center of each strip corresponding to zero position. At the early times this peak should appear only in the strips closest to the propellant surface. As time progressed smaller and broader peaks would be expected to appear in strips further from the propellant as the particle structures expanded and moved away from the original position that produced them and the decomposition structures on the propellant surface grew. Particles further away from the propellant surface would correlate with decomposition structures formed earlier on the surface, which would still be visible throughout the entire image sequence. None of the runs produced this ideal cross correlation. The run on the left of Fig. 18 is the closest the correlations came to matching the ideal. There is a peak, but it is offset to the left. Looking at Fig. 17, this seems to be caused by the bright particle structures near the surface to the right of center correlating with the bright decomposition structure in the center of the surface images.

It was common in the early images of all runs to find the strip closest to the propellant surface with high correlations along its entire length. The reason for this is the pixels in the top row in these scattering images have large signals due to bleeding from detector pixels viewing the propellant surface as well as a large amount of particles being created across the entire width of the propellant at this time. Also there is no correlation between the images at 636 μs because particles are not being produced at that time, and all the scattered particles were produced at an earlier time. Cross correlations between the surface ratio images and the laser scattering images were attempted as well. Correlation peaks would only be expected in the strips closest to the surface. However, very little correlation was found with these two image sets as well.

Another phenomenon observed with the laser scattering images was continued reaction and bubble formation well after the plasma discharge. Figure 19 contains an example sequence of images starting at a delay of 1036 µs and progressing to 10 ms.
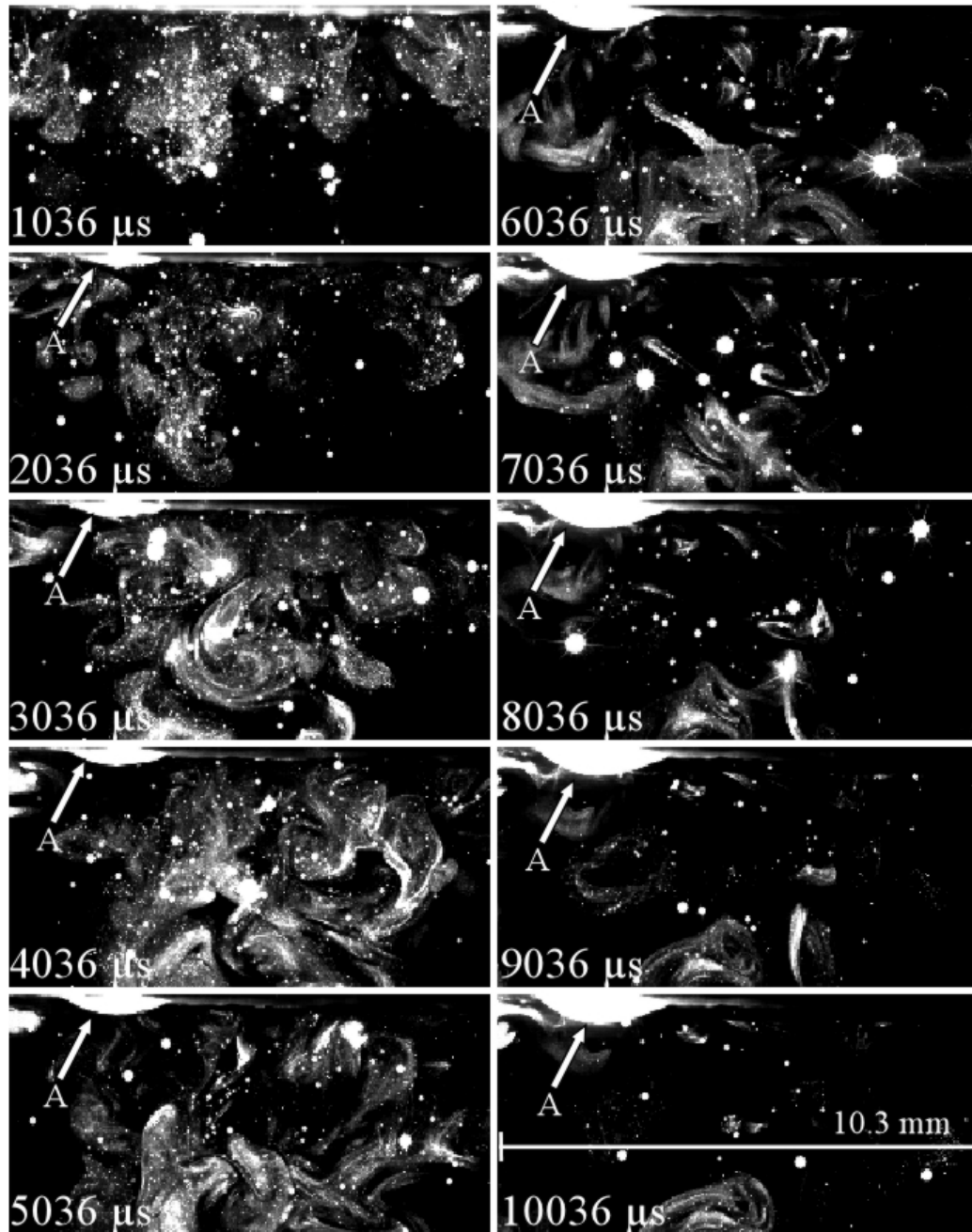
Figure 19: Example scattering image sequence after firing.

Two observations are made in this series. The first is a large bright region appearing and growing on the surface of the propellant during the sequence, labeled "A" in the figure. The bubble appears between 1 and 2 ms and grows steadily until 8 ms with a maximum width of about 2.6 mm. Bubbles are commonly seen growing out of the propellant surface after the plasma firing and are seen in all the scattering image runs. This image sequence is displayed because the bubble is so large; bubbles are usually about 1 mm in size. These bubbles are probably the larger blisters observed on the propellant surface after each firing. It is interesting that the laser

illuminates both sides of the bubble. This might be evidence that the structure seen is in fact hollow.

The second observation is that during this sequence the larger, more diffuse type of scattering structure appears. At 1 and 2 ms the particles are similar in structure to those in Fig. 16. However, at 3 ms some scattering structures appear that resemble the larger, brighter, more diffuse scattering structures seen in Fig. 8. These structures resemble an intermediate point in a scalar mixing process where the particle density is considered the scalar. This implies that at some point previously these particles were in a region of more uniform density and were then mixed with the air away from the propellant surface. The bubbles would presumably contain a relatively homogenous volume of fluid before bursting. Also, these structures coincide with the appearance of the bubbles on the surface, so it is possible that they are a result of exhaust from the bubbles.

One run was conducted using simultaneous imaging where the OD2 neutral density filter on the propellant surface camera with an OD 0.6 neutral density filter. This enabled viewing of the propellant surface over much longer times. A bubble did appear in the scattering images on this run, and Fig. 20 is a time sequence of close up views of the two camera images plotted on the same cross-plane view. The green strip across the surface images marks the laser. The bubble appears at 1516 μs and grows up to, and beyond, the end of the sequence at 2616 μs. It has been colored light-blue and labeled "A" throughout the sequence in Fig. 20. It appears on the figure below the laser strip because the top of the scattering images are actually offset from the original surface position and the cross-plane figures are viewed at an angle. The changes on the propellant surface do track with the formation of the bubble in the scattering images. The propellant continues to decompose throughout the time sequence, and there are lighter regions on the surface where the bubble is lowest, with darker regions where the bubble surface dips. However, there is nothing in the surface images alone to obviously mark that region as bubbling outwards. This does suggest that there is some three dimensionality associated with all the changes taking place on the propellant surface.
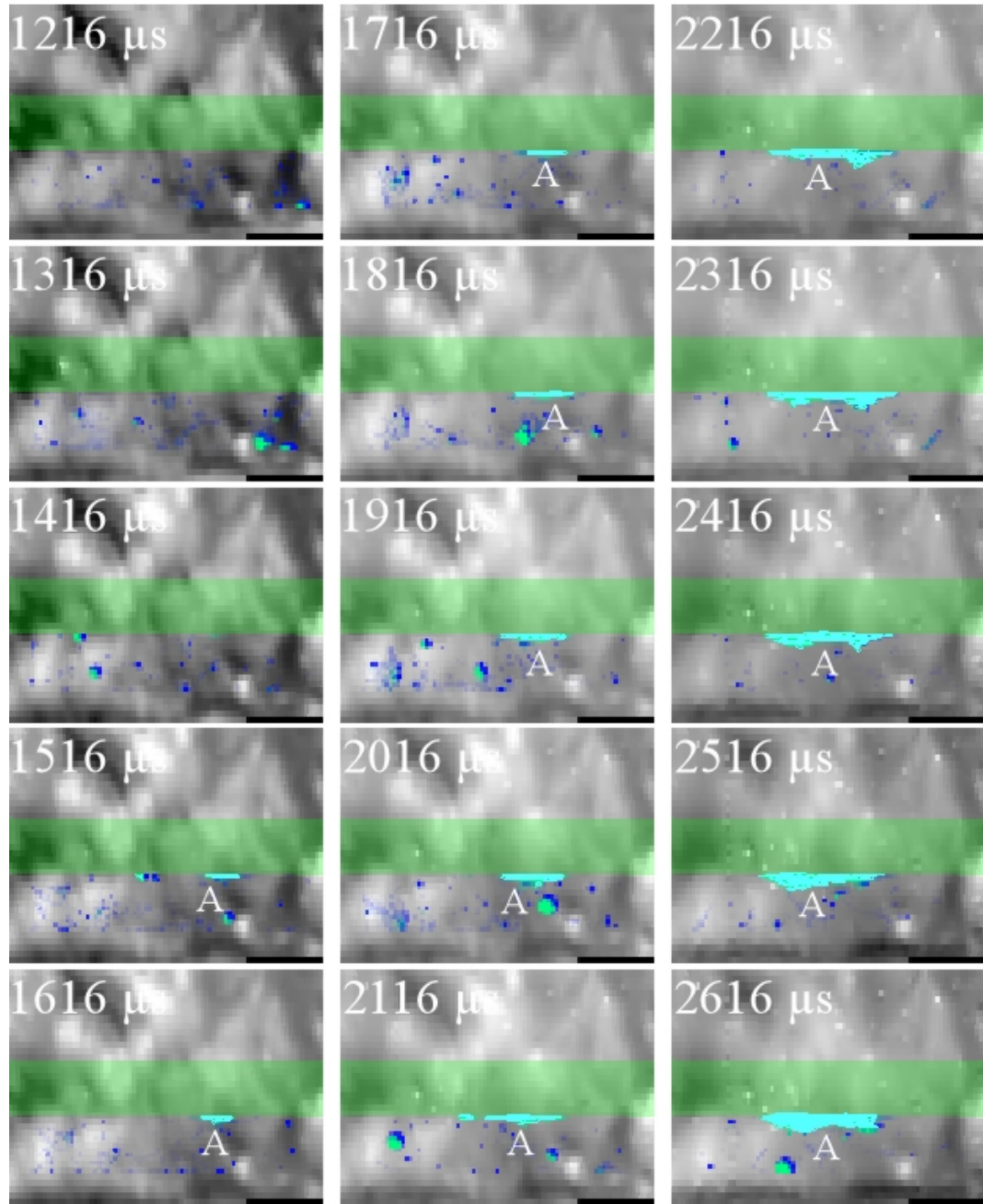
Figure 20: Time sequence of close up view of bubble growing with corresponding propellant image. Bubble has been false colored light-blue and labeled "A".

Bibliography

Beyer, R., Pesce-Rodriguez, R., 2000. "Experiments to Define Plasma-Propellant Interactions," IEEE Trans. Magnetics, vol. 39, p. 207.

Beyer, R. Pesce-Rodriguez, R., 2004. "The Response of Propellants to Plasma Radiation," ARL-TR-3189, U.S. Army Research Laboratory, Aberdeen Proving Ground, MD.

Kappen, K. Beyer R., 2003. "Progress in Understanding Plasma-Propellant Interaction," Propellants, Explosives, Pyrotechnics, vol. 28, no. 1, p. 32.

Kim, J., Clemens, N.T., Varghese, P.L., 2002. "Experimental Study of the Transient Underexpanded Jet Generated by Electrothermal Capillary Plasma," AIAA J. Propulsion and Power, vol. 18, no. 6.

Kimura, J., 1988. "Kinetic Mechanism on Thermal Degradation of a Nitrate Ester Propellant," Propellants, Explosives and Pyrotechnics, vol. 13, p. 8.

Kohel, J.M., Su, L.K., Clemens, N.T., Varghese, P.L., 1999. "Emission Spectroscopic Measurements and Analysis of a Pulsed Plasma Jet," IEEE Trans. Magnetics, vol. 35, p. 201.

Koleczko, A., Ehrhardt, W., Kelzenberg, S., Eisenreich, N., 2001. "Plasma Ignition and Combustion," Propellants, Explosives, Pyrotechnics, vol. 26, p. 75.

Kovesi, P., 1999. "Phase Preserving Denoising of Images," The Australian Pattern Recognition Society Conference: DICTA'99, Perth, Western Australia, pp 212-217.

Lieb, R., Kaste, P., Birk, A., Kinkennon, A., Pesce-Rodriguez, R., Schroeder, M., Del Guercio, M., 2001. "Analysis of Burning Rate Phenomena and Extinguished Solid Propellants from an Interrupted Closed Bomb with Plasma Igniter," ARL-TR-2561, U.S. Army Research Laboratory, Aberdeen Proving Ground, MD.

Seitzman, J.M., ©1985-1990. "Lines," "Spectra," Version 3.0, High Temperature Gasdynamics Laboratory, Mechanical Engineering Dept., Stanford University.

Appendix

An electrothermal plasma was produced in a capillary discharge using an apparatus very similar to that of Kohel et al. (1999) and Kim et al. (2002) with a 251µF capacitor discharging through the capillary with a 25µH inductor to stretch the pulse length. In all the experiments in this study the capacitor was charged fully to 5 kV. The plasma did not make direct contact with the propellant surface in these experiments; only radiation from the plasma reached the propellant surface. A chamber was bolted onto the plasma producing device to capture the plasma jet. This increased the residence time and density of the plasma in front of the propellant over that of an open air firing. Both of these effects would cause an increase of radiative energy transferred to the surface of the propellant. In order to minimize the metal deposition inside the chamber and capillary, the plasma exhausted during the firing through a 3 mm diameter vent in the side of the chamber. The plasma was not completely confined, and the capacitor discharge lasted up to 100 µs longer than in an open air discharge.

Figure A-1 shows the setup of the capillary enclosure along with the plasma chamber for a typical laser diagnostics experiment for a plasma radiation-propellant interaction. A 1.27 cm diameter disk of JA2 propellant (0.05% graphite by weight) punched from a 2.54 mm thick sheet was fastened by a coating of Vaseline to the bottom of a steel rod above the chamber window before each firing. The side surface facing the camera was coated with a lamp black solution to minimize the luminosity from the propellant and to improve visibility of the signal just above the surface. The bottom surface of the propellant was 2.70 cm from the bottom edge of the plasma chamber window during the initial NO PLIF and particle scattering experiments. In the simultaneous high speed imaging experiment the propellant was moved to 3.14 cm offset from the plasma chamber to enable a view of the propellant surface.
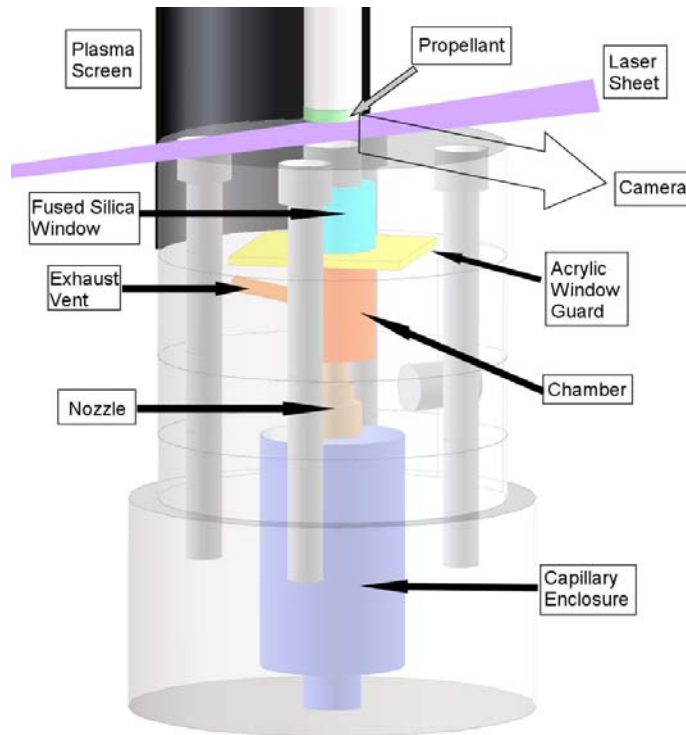

Figure A-1: Capillary enclosure and discharge chamber with window for plasma radiation.

The plasma was produced inside the capillary, propagated through the nozzle, and then expanded into the chamber (5.8 cm^3). The plasma was completely isolated from the propellant by a 1.27 cm thick fused silica window on the top of the chamber. This window was protected by a 1.59 mm thick disposable clear acrylic sheet for the initial imaging experiments. Both the acrylic sheet and a fused silica flat of the same thickness were used to protect the window during the two camera high speed imaging experiment. This enabled an observation of the effect of added ultraviolet radiation to the broadband visible radiation that decomposes the propellant when using the acrylic mask. A blackened aluminum foil screen was attached to the chamber wall to block the camera's view of the plasma exhaust so no background luminosity from the plasma was observed.

Two data sets were taken to characterize the plasma radiation through the chamber window. The radiation intensity time history during a firing was measured using a fast response photodiode put in place of the propellant with an ND 200 filter attenuating the light. Also, the emission spectrum was measured at two different times during the discharge with an acrylic window guard. A fused silica lens focused plasma light onto a 100 μm fiber optic, spectrally resolved by a Spex 1681 spectrograph with a 50 μm slit width and recorded on a Roper Scientific PI-Max intensified CCD camera. The camera was gated to 1 μs and only one spectrum was taken per firing because image acquisition time was much greater than 600 μs. However, the spectra were repeatable enough that multiple spectra taken over different spectral ranges at a given delay could be spliced together to form an emission curve.

Figure A-2: NO PLIF laser setup.

SINGLE SHOT NO PLIF AND PLMS IMAGING

Figure A-2 shows the laser setup for the NO PLIF experiment. Several steps were needed to create the 226 nm light needed to pump NO. A frequency doubled Nd:YAG (Spectra Physics GCR 150) laser pulsed at 10 Hz and operated at 532 nm was used to pump a Lumonics HyperDye-300 laser. The dye laser, with a 2×10-4 molar concentration of Pyromethene 597 dissolved in ethanol was tuned to output a 574 nm beam. The 574 nm beam was then frequency

doubled with a KDP crystal inside an Inrad Autotracker II. The resulting 287 nm light is combined with the residual 1064 nm light from the Nd:YAG that has been time delayed to coincide with the dye beam by lengthening the laser path across the table. The combined beams were then mixed in a KDP crystal inside a second Inrad Autotracker II to create the 226 nm beam. This beam was separated from the residual 1064 nm and doubled dye beams with a fused silica Pellin Broca prism which also steered it to the plasma chamber. The ~1 mJ laser pulse was focused with a 1 m focal length fused silica lens and then expanded into a sheet using a 25.4 mm focal length cylindrical lens. The cylindrical lens was placed only 7-8 cm from the propellant because the field of view was only 5 mm tall. A photograph of the camera and plasma chamber geometry is shown in Fig. A-3.
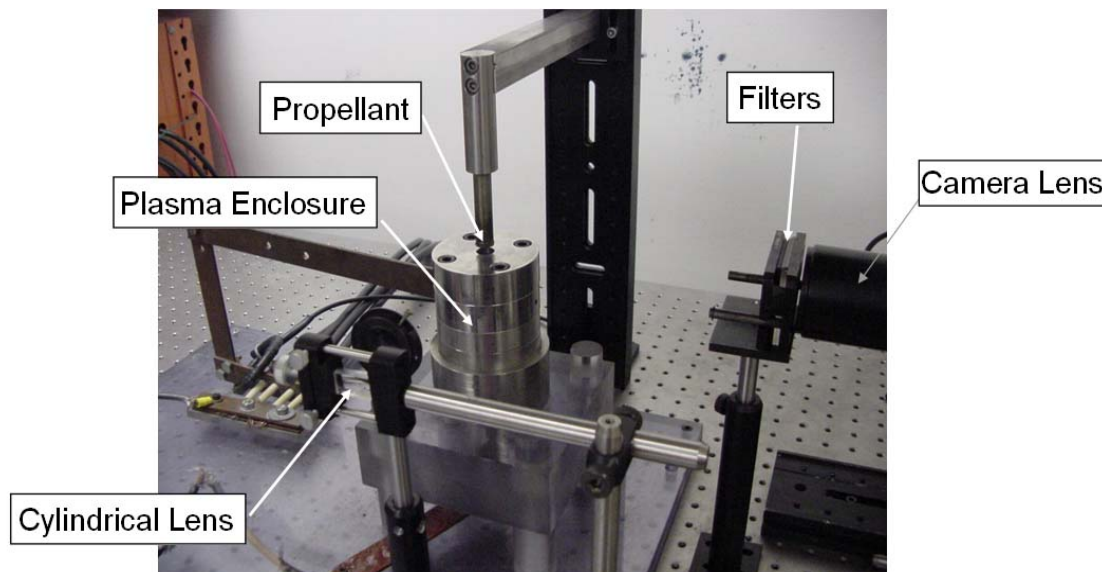

Figure A-3: Photograph of the NO PLIF and Nd:YAG PLMS experimental setup.

The first excited electronic transition of NO, $A^2\Sigma^+(v'=0) \leftarrow X^2\Pi(v''=0)$ was employed for fluorescence imaging. The dye laser wavelength was calibrated by an excitation scan. The laser was scanned across the rovibronic absorption lines of NO at a rate of 0.0004 nm/s and the broadband fluorescence signal was collected through a UG5 filter onto a Hamamatsu PMT. A Stanford Research Systems 250 Boxcar Averager/Gated Integrator was used to collect the fluorescence signal synchronous with the laser pulses. The fluorescence signal was averaged over 30 pulses and the averaged signal was collected by a Tektronix TDS 520C digital oscilloscope as the laser was scanned. This measured absorption spectrum was compared to a calculated spectrum (Seitzman 1985-1990). The $Q_{21}+R_{11}(9.5)$ transition pair at 225.9802 nm was chosen as the pump for PLIF because it produced a relatively large signal. There was no estimate of the temperature of the NO exiting from the propellant. However, the heat flux gauge temperature only increased tens of degrees during plasma impingement. Therefore it was thought that the absorption line that produced high signals at room temperature was thought to be adequate for pumping during the plasma radiation-propellant interaction.

Fluorescence imaging was conducted using a Roper Scientific PI-Max 512 intensified CCD camera. A UG-5 UV filter was placed in front of the Nikkor Nikon UV lens to attenuate laser light scattered onto the CCD. The field of view geometry is shown in Fig. 3. The diameter of the propellant disk at the top of the image was 12.7 mm wide. The propellant was located 5 mm from the top surface of the plasma chamber, which was cropped from the bottom of the image. During the firings the propellant surface was never exactly flat and changed over time during the

interaction as material was lost from the surface. Because the laser pulse period and camera readout time was much longer than the plasma discharge time of 600 μs, only one image was taken per firing. A series of NO fluorescence images were taken from 100 μs delay from the plasma trigger (when NO first began to appear) to 600 μs (when the capacitor finished discharging) at 50 μs time intervals. Usually two to three images were taken at each time delay. Although NO was present after 600 μs, we were not interested in the conditions after the plasma discharge.

While conducting the fluorescence experiments, a small amount of scattering off large particles was seen throughout the flow. This warranted further study and a scattering experiment using the frequency doubled Nd:YAG was conducted. The same intensified CCD camera was used, this time looking through OG 515 and BG 38 filters to attenuate luminosity from the propellant surface. The ~20 mJ/pulse laser was apertured to 5 mm high and formed into a sheet by a 225 mm convex cylindrical lens. This was different than the NO experiment because the laser power was much higher and the original beam was much larger as well.

SIMULTANEOUS HIGH SPEED PROPELLANT IMAGING AND PLMS

Figure A-4 is a photograph of the experimental setup for the two camera simultaneous high speed video of the propellant surface and laser scattering by ejected particulates. This experiment employed the same plasma radiation chamber as in the single shot NO PLIF and PLMS experiments. The propellant was raised to 3.14 cm above the plasma chamber to enable viewing of the propellant surface. A Coherent Evolution 90 Nd:YLF laser pulsed at 10 kHz was used as the light source. The laser was run at full power during the scattering experiment (nominally 90 W, 9 mJ per pulse). The beam from the laser seen in the bottom left of the image was steered towards the propellant by two 45º mirrors. The beam was apertured on the top by a beam stop before being formed into a sheet by a 250 mm focal length cylindrical lens. The aperture was to keep the laser from igniting the propellant.
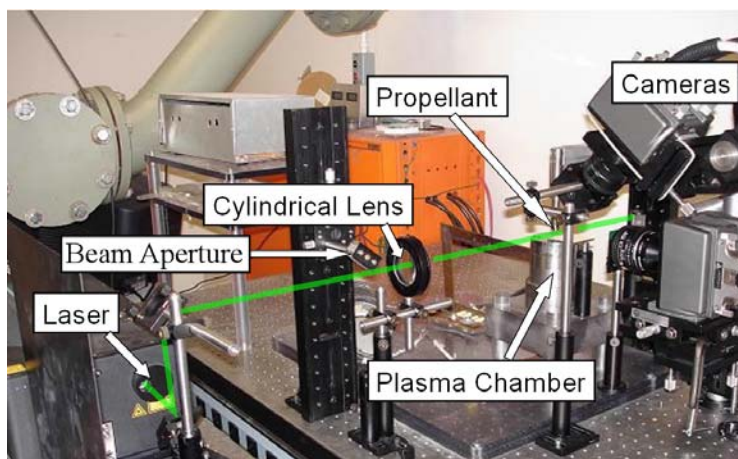

Figure A-4: Experimental setup of the two camera simultaneous imaging experiment.

Two Photron Fastcam Ultima APX cameras were used to conduct high speed imaging. The propellant surface camera was run at a frame rate of 50 kHz while the laser scattering camera was run at 10 kHz. At these high speeds, the detector size was 256×64 and 256×128 pixels, respectively. There were problems with the capacitor discharge interfering with the readout for the 10 kHz camera, and so the detector size was reduced from the maximum the camera could handle at that frame rate.

A close-up photograph of the camera setup is shown in Fig. A-5. The scattering camera was in the same position as the ICCD camera in the previous experiments. It viewed laser scattering through a bandpass filter that attenuated scattering of the broadband plasma emissions. The surface camera was mounted at an angle looking down towards the top surface of the plasma chamber. A broadband visible mirror was placed on top of the plasma chamber so that the camera viewed the bottom surface of the propellant disk. Because the camera was at an angle, the lens was mounted on a Scheimpflug mount, and had lens extension tubes to enable a smaller field of view. The Scheimpflug mount tilts the lens with respect to the detector plane so that the plane of focus is at an angle with respect to the detector plane. The lens was set to f/16 so the entire propellant surface was in focus, and a neutral density (OD 2) and a colored glass filter (OG 550) were used with this camera. The attenuation provided by the neutral density filter enabled viewing of the propellant surface during the plasma firing (the surface was illuminated only by the plasma), and the OG 570 further attenuated the UV light scattered by the propellant when the fused silica mask was in use. Five images of laser scattering were recorded during the plasma discharge, with 100 successive images recorded for the run. About 40 successive images of the propellant surface were visible using the specified propellant surface camera setup. The shutter time for both cameras was set to 4 μs. The cameras were run slightly out of sync to avoid laser scattering appearing in the propellant surface images and registered in order to correlate events on the surface with particles appearing below the propellant.
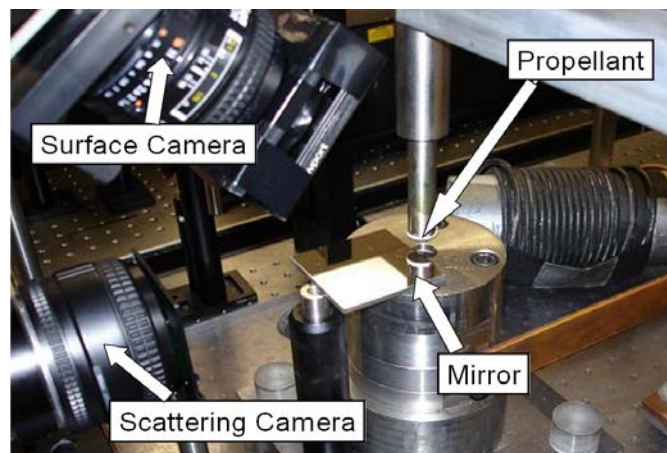

Figure A-5: Close up view of two camera simultaneous imaging experiment.

Figure A-6 shows the size and geometric relation of the fields of view for both cameras. The method of viewing simultaneous images of two different planes on the same plot is explained. Part a) shows the point of view of the observer for all the cross-plane plots in this work. Part b) shows an example plot in relation to the two surfaces with fields of view dimensioned. The laser sheet is perpendicular to the propellant surface and translates across the middle of the propellant surface camera field of view. Both surfaces are marked in the figure. The field of view for the cameras was only 10.3 mm wide, smaller than the 12.7 mm propellant disk diameter, and the width of the patch of propellant surface viewed by the camera is 3.2 mm.. The laser scattering camera views the area 5.1 mm below the propellant surface.
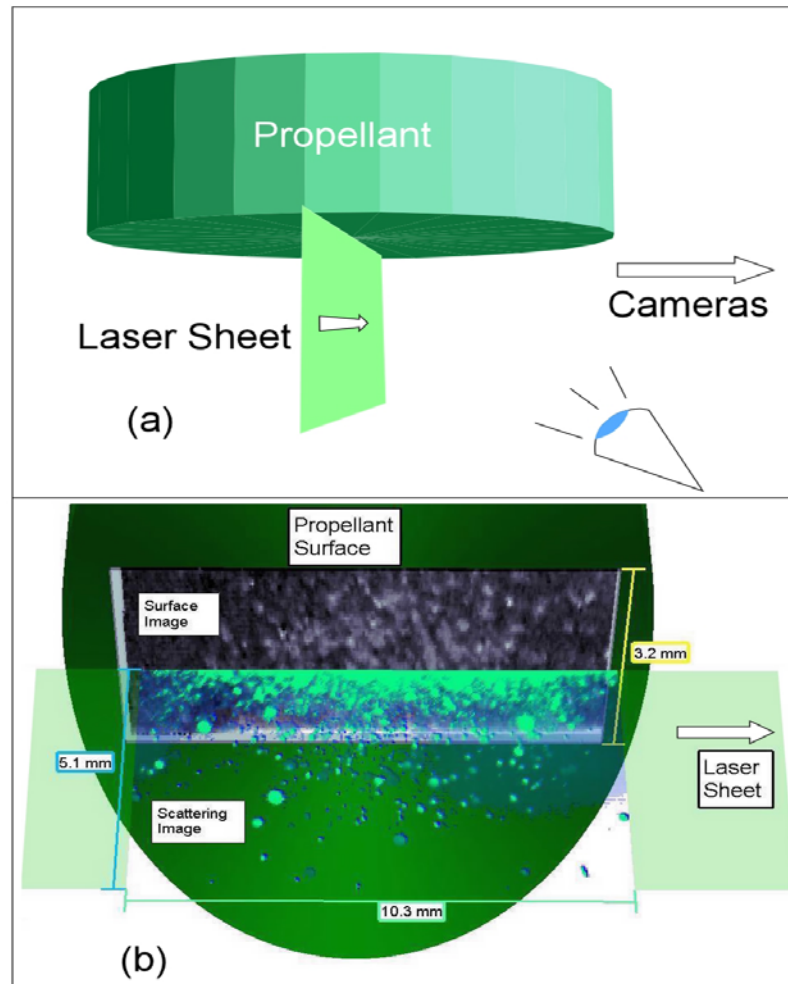
Figure A-6: Field of view geometry for both cameras a) Diagram of observer position for cross-plane plots b) Relationship of the camera fields of view for scattering and surface images.